CrossMark

Morphological study of branched Sn structure formed under selected electrochemical conditions

Hanan Teller[1], Shani Ohanona[1], Diwakar Kashyap[1], and Alex Schechter[1,*]

[1] Department of Chemical Sciences, Ariel University, Ariel 40700, Israel

ABSTRACT

A controlled electrodeposition process of branched micrometric and nanometric metallic tin structures was developed. Selected potentiostatic and galvanostatic techniques were explored with the aim of forming hierarchical shaped Sn on carbon porous electrodes by a simple template-free synthesis. We have studied the influence of continuous potential steps ranging from -0.9 to -4 V versus Ag/AgCl which show a classical nucleation growth mechanism. Under high overpotentials above -1.5 V, the reaction is governed by mass transport, which enables the development of vertically aligned dendrites. Upon reaching a dendrite particle size of 2–5 μm, Sn^{2+} reduction is facilitated on branches extending at an angle of about 45° from the main stem due to enhanced spherical diffusion to these newly evolving sites. A competing reaction of hydrogen evolution plays a significant role during initial nucleation stages and throughout particle evolution by reducing the overall columbic efficiency. Further study of means to affect the mass transport and morphology has led us to investigate the influence of pulse deposition duty cycle as well as use of anionic (SDS—sodium dodecyl sulfate) and cationic (HDTAB—hexadecyltrimethylammonium bromide) surfactants. While short pulses and long rest time promote the formation of high surface density of small nuclei, surfactants directly influence the tin ions (SDS) or adsorbed on the negatively charged electrode (HDTBA). Finally, the study of an electrodeposition method using strong acid additives was developed. It is shown from SEM and EQCM studies that careful selection of the acid type and concentration gives rise to the formation of a much more advanced network structure promoted by selective etching and co-reduction of dissolved ions. Highly interesting two-dimensional tin films formed in this process are also reported.

Address correspondence to E-mail: salex@ariel.ac.il

Springer

Introduction

Nano- and microstructured tin and tin oxide have drawn the attention of the scientific community owing to their unique three-dimensional architecture, high surface area, and enhanced electrical conductivity which differ greatly from those of their bulk [1]. Materials based on Sn particles have many important applications related to energy storage in supercapacitors [2] and Li-ion battery electrodes [1, 3], in soldering and electronic assemblies as Sn-rich alloys [4, 5], and as photocatalysts (e.g., Sn–SnO$_2$/C) with visible light activity [6, 7]. Tin oxides have already been demonstrated in new-type chemical sensor arrays for detection of many gases [8, 9]. Tin dioxide has been used for the design of new nanoscaled electronic devices such as nano-FETs (field effect transistors) that are fully transparent [10].

However, the production of the small surface structures often involves complicated multistep and costly procedures (e.g., chemical vapor deposition [11]). In addition, uniform dispersion of the nanostructures on large surfaces remains a challenge.

Electrodeposition is a preferable way to form metallic microscopic structures with diverse dimensions, morphologies, and crystallinities [12]. For example, micro- and nanowires, as well as nanofibers, were prepared on selected substrates used as templates including polycarbonate membranes [13], carbon nanotubes [14], and hard support such as alumina [15]. Nevertheless, the use of templates is somewhat problematic due to limited mechanical and chemical stability of polymeric templates, which restricts the removal of the particle without damaging the prepared material. This shortcoming can be addressed by applying electrodeposition methods under selected conditions.

Electrochemical plating of metallic electrodes has been widely reported [16–18]. The morphology of the electrodeposited particles strongly depends on an array of conditions [19–21] applied in the process. In general, the variation in the morphology depends mostly on the interplay between the crystal growth rate and the mass transport rate of reactants to the metal–solution interface. For example, at large overpotentials, where the reaction rate is diffusion controlled, dendrites are formed due to ion deficiency near the electrode under primary current distribution reduction control. At low overpotentials, the electrodeposition is governed by nucleation grain formation followed by lateral growth in an activation-controlled process which leads to a more uniform coating [22, 23]. In addition, at high overpotentials (or high current densities), hydrogen evolution on the electrodes can become the main charge-consuming process [24]. Other parameters influencing the deposition have been reported, including the plating bath composition, pH, temperature, solvents, and complexing additives [25].

Few research groups have published reports on electrodeposition of metallic tin nanostructures [26–30]. Hen et al. studied the influence of solution composition on the electrodeposition of Sn from Sn(II)–citrate (Sn–Cit) solutions at low overpotentials. The authors identified [Sn–HCit]$^-$ as the main species at a pH of about 4 which is associated with an increase of the deposition onset potential [26]. Hong et al. reported the formation of highly porous Sn foam by galvanostatic deposition at an extreme current density of -3 A/cm^2 on copper foil in a solution containing sulfuric acid and SnSO$_4$ [27]. Recently, the formation of tin nanowire arrays was reported from two ionic liquids by template-assisted electrodeposition process using polycarbonate membranes as templates at -0.5 V [29]. The polymer template was removed by washing the electrode in dichloromethane. A template-free electrochemical synthesis of tin nano-needles was reported by Mackay et al. The authors used a copper substrate and sodium stannate in sodium hydroxide solution, and applied a constant potential of -2.4 V at 55 °C. Disoriented 1D needle-shaped Sn particles of 1–5 μm in length with a tip width of 20–100 nm and a base width of 50–300 nm were observed in their study [30]. Recently, Norton and Oven showed the effect of solution stirring and convective heat transport on the electrodeposition of tin nano-needles in alkaline solutions [31]. Tin nano-rods with a typical length of 500–700 nm and a diameter of 50–70 nm were synthesized by a surfactant-assisted technique [28].

In this paper, we present methods of controlling the electrodeposition process of metallic tin with the aim of forming a three-dimensional hierarchical shaped ("nanotrees") Sn layer on a porous carbon substrate. Different parameters influencing the morphology of the electrodeposits such as the electrodeposition potential or current, hydrogen evolution, and ionic organic additives are described. Finally, we address the effect of acids on the morphology and

stability of an electrodeposited Sn layer formed on a porous carbon structure.

Experimental

Sn micro- and nanostructures were electrodeposited from a stock solution of 18 mM $SnCl_2$ (99.99 % Aldrich) in ultrapure water (18 MΩ cm at 20 °C). 50 mM sodium citrate (Merck) was added as a stabilizer. In some solutions, hexadecyltrimethylammonium bromide (HDTAB, Sigma >98 %) and sodium dodecyl sulfate (SDS, Acros 85 %) surfactants were added. A constant charge was applied potentiostatically at the selected potentials in the range of −0.9 to 4.0 V, and galvanostatically at the current densities of 25–200 mA/cm², using Biologic VSP multichannel potentiostat. Sn was electrodeposited on Toray™ TGPH-090 carbon paper (1 cm²) in a standard 3-electrode cell equipped with a Pt gauze counter electrode and Ag/AgCl reference electrode. All deposition processes were performed under an inert nitrogen atmosphere in magnetically stirred solutions (500 rpm) at room temperature. The prepared electrodes were rinsed with water, dried, and then stored under nitrogen.

Diffusion coefficient measurements were performed on a 5-mm-diameter gold disk electrode (Pine Instruments) in standard a 3-electrode cell with Pt gauze as a counter electrode and Ag/AgCl electrode as a reference electrode (0.215 ± 0.005 V vs. normal hydrogen reference electrode).

QCM/EQCM measurements were performed using a CHI 408A electrochemical analyzer in a 3-electrode Teflon cell using a gold-plated quartz crystal electrode as a working electrode, Pt wire as a counter electrode, and Ag/AgCl as a reference electrode.

Scanning electron microscopy (SEM) measurements was performed on a JEOL GSM-6510LV system. The images were collected using secondary electron imaging (SEI) and backscattered electron composition (BEC) detectors. The structure of the electrodeposited Sn samples was characterized by X-ray diffraction (XRD) using a PANalytical X-ray diffractometer (X'Pert PRO) with Cu Kα radiation ($\lambda = 0.154$ nm) and phase analysis identification at 40 kV and 40 mA. Full pattern identification was carried out with the X'Pert High Score Plus software package, version 2.2e (2.2.5) by PANalytical.

Inductively coupled plasma (ICP) measurements were performed using a Varian EIS 710 system.

Results and discussion

Voltammetric properties

The standard reduction potential of the Sn^{2+}/Sn couple is −0.137 V versus NHE. It is well known that Sn ions tend to form oxides in aqueous solutions with pH > 1. Therefore, a complexing agent, typically citrate salt, was added to ensure the solubility of the Sn^{2+} ions. Figure 1 shows the steady-state voltammogram of a gold electrode in 18 mM Sn^{2+} and 50 mM sodium citrate solution (pH 6). As reported before, the electrodeposition occurs at −0.55 V, which is significantly more negative than the Sn^{2+}/Sn redox potential. This behavior is attributed to the formation of stable Sn–citrate complexes [26]. Under these cathodic potentials, the diffusion-controlled current reaches a maximum at −1 V, followed by a gradual decrease of the current seen in more negative potentials. An emerging new process seen from −1.25 V is ascribed to hydrogen evolution. The small anodic peak at around −0.3 V is assigned to Sn dissolution as determined by EQCM measurements (not shown). It should be noted that the dissolution process at pH 6 is hindered by the formation of a tin oxide passive layer that assures the stability of the deposited Sn [32].

The lowering of electrodeposition potential below −1.5 V results in the formation of sub-micron tin dendrites with branched architecture. Figure 2a
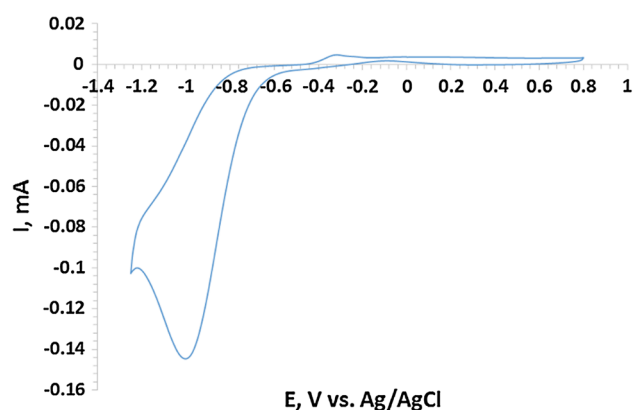

Figure 1 Current–potential curve of Sn electrodeposition on a gold disk electrode (18 mM $SnCl_2$/50 mM sodium citrate solution; scan rate: 10 mV/s).
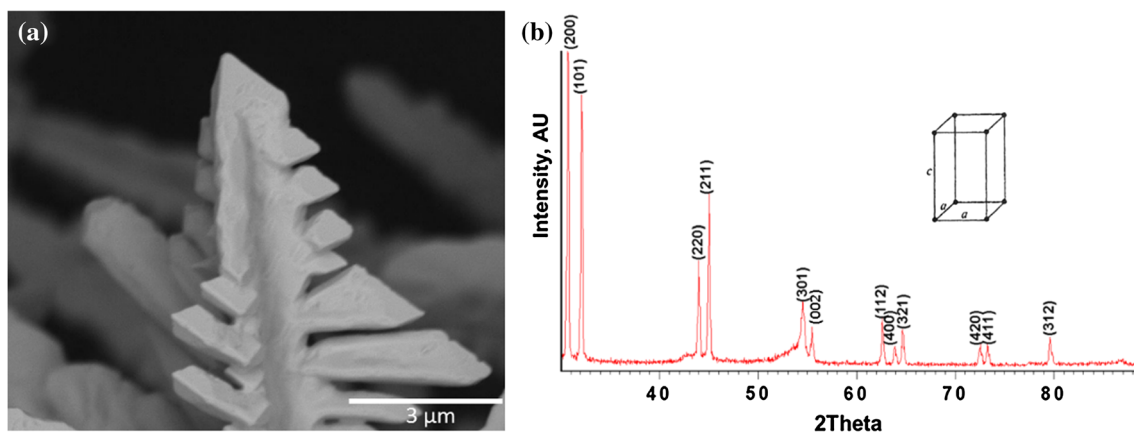
Figure 2 HRSEM micrograph (**a**) and XRD pattern (**b**) of tetragonal β-Sn electrodeposited dendrites (18 mM SnCl$_2$ and 50 mM sodium citrate solution, −3 V).

displays a SEM micrograph image of tin branched structure (TBS) grown on the carbon substrate at −3 V. The TBSs are connected on one side to the electrode and extend towards the solution on the other side. The nanometric branch/sub-branch image of a single TBS reveals a high degree of ordered morphology both of the stem and its branches. The XRD pattern in Fig. 2b explicitly shows the formation of a single-phase β-Sn that preserves the tetragonal structure. The crystal structure of TBS was analyzed from the XRD pattern of the particles that grow in different orientations on the carbon electrode surface. It should be noted that the facet pairs with the strongest intensity [200], [101], [220], and [211] (Fig. 2b) are oriented at an angle of 45° with respect to each other, in line with the position of many observed branches, with respect to the steam.

The growth of Sn was studied at constant applied potential in the diffusion-controlled region. Diffusion of Sn^{2+} ions to the electrode, at potentials more negative than −1.5 V, governs the kinetic of TBS growth in the plating bath. Mild stirring of the solutions further increases the deposition currents in potentiostatically controlled experiments. We have found that magnetic stirring at 500 rpm is a good balance between improving the mass transport and preventing the detachment of long nanotrees from the surface, occurring under vigorous stirring.

Growth under constant potentials

In general, the electrodeposition process proceeds via nucleation–adsorption–growth–branching–growth of the deposited metal [33]. Manifestation of this growth

mechanism is seen in Sn nanotree formation in Fig. 3. SEM images were collected from electrodes during polarization to −3 V at different stages during the growth process. After 20 s, two typical deposits are observed: one with the average dimensions of 125×125 nm and larger size particles of 700×250 nm (Fig. 3a). A continuation of the reduction leads to further nucleation in parallel with the growth and branching of the dendrites. A stem-like shape starts to appear, thus leading to an increase in the particle size to 2×0.5 μm after 30 s and 5×1 μm after 60 s (Fig. 3b, c, respectively). A comparison between TBS dimensions attained after 300 s and after 600 s shows a typical increase of the stem dimensions from 35 to 80 μm in length and 1 to 2.5 μm in width (Fig. 3d, e). Interestingly, the aspect ratio of 32–35 (stem length/width) was maintained throughout the particle growth evolution. Visual inspection of the branch length and width shows an increase from 2 to 8 μm and from 0.65 to 1.2 μm, respectively. Hence, branches seem to increase much faster in length than in their diameter. The growth of branches succeeds the nucleation process, which exposes active crystal facets. Further growth on different facet planes leads to the formation of diffraction planes shown in Fig. 2. These planes differ in their surface energy, resulting in the growth in selected orientations and not in all directions as reported by a few others using similar electrodeposition methods [30, 34].

It is generally accepted [22, 23] that after formation of Sn nuclei, a protrusion starts to propagate on the surface of the electrodes. Linear diffusion of Sn^{2+} proceeds towards the flat planes of the protrusion,
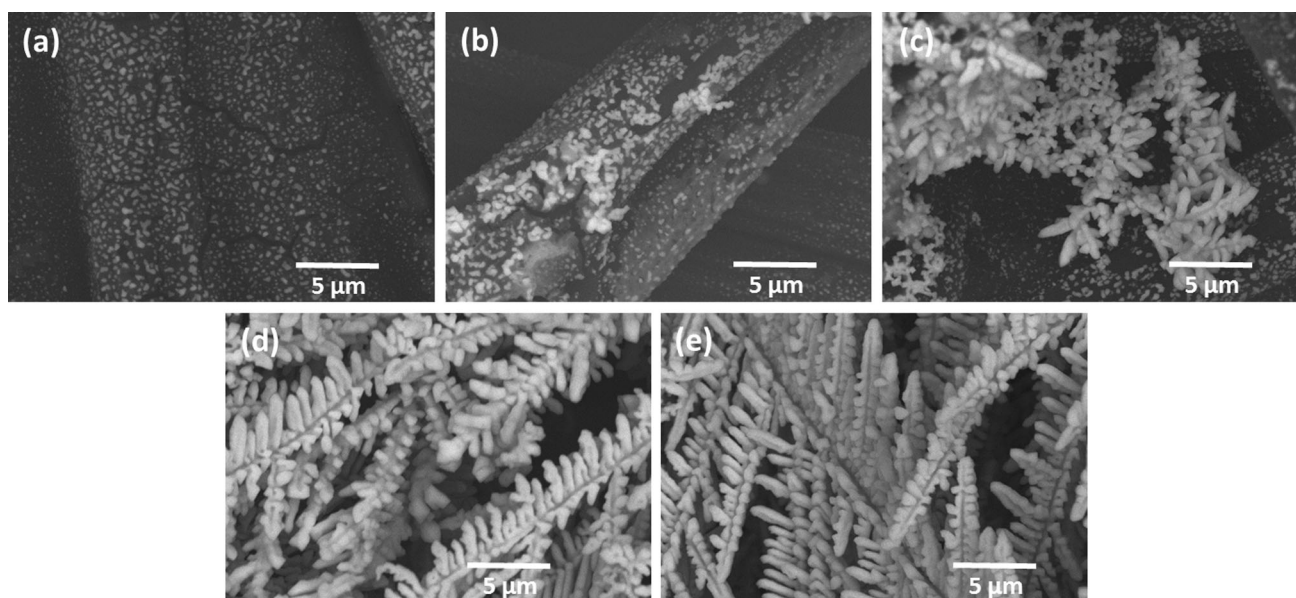
Figure 3 SEM micrographs of Sn electrodeposition at −3.0 V after **a** 20, **b** 30, **c** 60, **d** 300, and **e** 600 s.

whereas spherical diffusion occurs near the curved tips. Due to the faster spherical diffusion, elongation of the dendrite is more dominant. However, it seems that when the stem thickness reaches a critical value, the spherical diffusion becomes less dominant and the aspect ratio as a function of time remains constant [35]. Yet, in the case of thin branches, the fast spherical diffusion remains pronounced, thereby promoting the increase of aspect ratio over time.

The effect of applied potential on the TBS morphology was studied in the range of −0.9 to −4.0 V versus Ag/AgCl, corresponding to kinetics through mass transport activation. Under negative potentials below −1.5 V, hydrogen evolution reaction (HER) competes with the parallel metal reduction despite the fact that HER on tin surfaces proceeds at much higher potentials (−1.72 V vs. SHE) than on Au, Pt, and Ni [36]. Under more negative potentials, the charge associated with this reaction strongly affects the electrodeposition coulombic efficiency (Fig. 4).

Electrodeposition efficiency of Sn was measured as a function of applied constant potentials limited by a predetermined total charge of 10 C. The efficiency was calculated from the weight difference before and after the Sn plating and was verified by ICP analysis. Figure 4 depicts an exponential decrease of the efficiency with the increase of applied overpotential. The immense HER (up to 96 %, at −4 V), formed both on Sn nanotrees and Toray^{TM} carbon substrate surfaces,
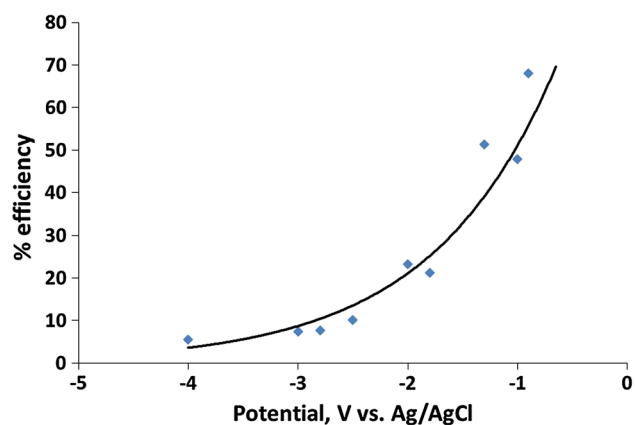

Figure 4 Sn electrodeposition efficiency versus deposition potential (18 mM $SnCl_2$ and 50 mM SDS, total charge: 10 C).

consumes most of the charge and forms bubbles which perturb the deposition. In addition, these bubbles limit Sn^{2+} diffusion, hence promoting dendritic structure formation. Similar effects on the morphology of copper electrodeposited in acid solutions (pH ≤ 0.3) were reported previously by Nikolić et al. [24].

Figure 5 shows the morphology of deposited Sn on Toray carbon paper prepared within the above potential range and a limited charge of 10 C. The particles formed at the lower potentials of −0.9 V and −1.3 V (below −1.5 V) show mostly lateral growth in the size of the nucleation grains and smooth facets.
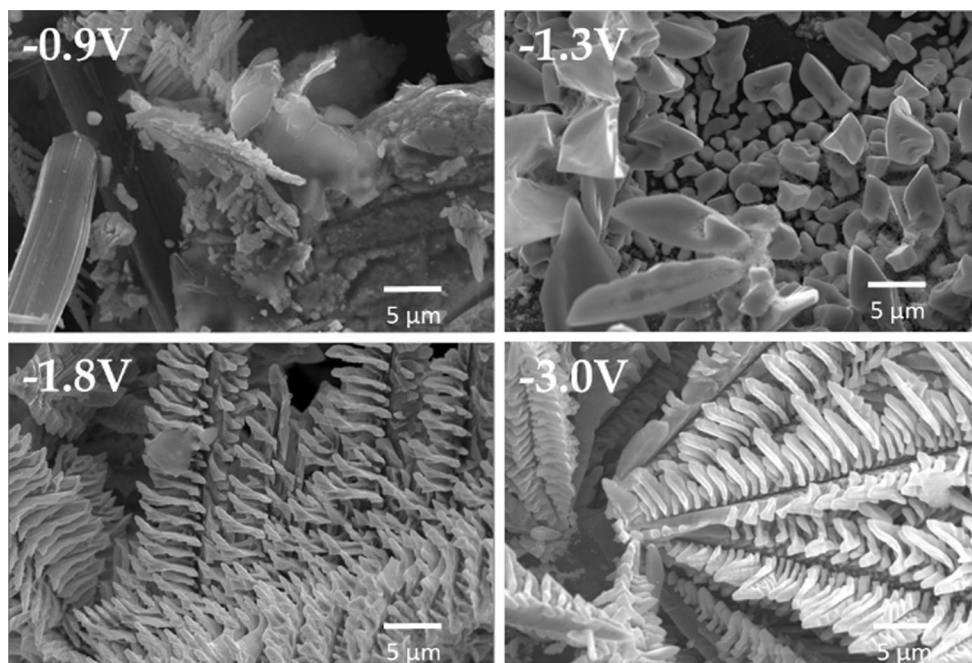
Figure 5 SEM micrographs of electrodeposited Sn at different potentials: **a** −0.9 V, **b** −1.3 V, **c** −1.8 V, and **d** −3.0 V (18 mM SnCl$_2$/50 mM SC solution, total charge: 10 C).

Hierarchical dendritic growth occurs at −1.8 V (above −1.5 V), in accordance with the low efficiency and intense hydrogen evolution at these potentials presented above. Interestingly, the nanotrees developing under −1.8 V (Fig. 5) have wide branches, aligned both horizontally and vertically, and have higher surface coverage. Conversely, the surface coverage of nanotrees prepared using −3 V shows distinct gaps between the nanotrees. This morphology is attributed to hydrogen evolution, which restricts the nucleation step on the carbon substrate, due to blocking of its surface by the evolved hydrogen bubbles, and confines its successive dendrite growth to these nuclei where the hydrogen evolution is less pronounced due to the relatively high overpotential of hydrogen evolution on Sn [36]. Strong diffusion dependence growth and low charge utilization efficiency at this potential facilitate the elongation of the narrow branches.

Electrodeposition under constant currents

We further studied the effect of galvanostatic control conditions on TBS morphology. Sn electrodeposition was performed using selected constant current density values and was limited by a total charge of 15 C
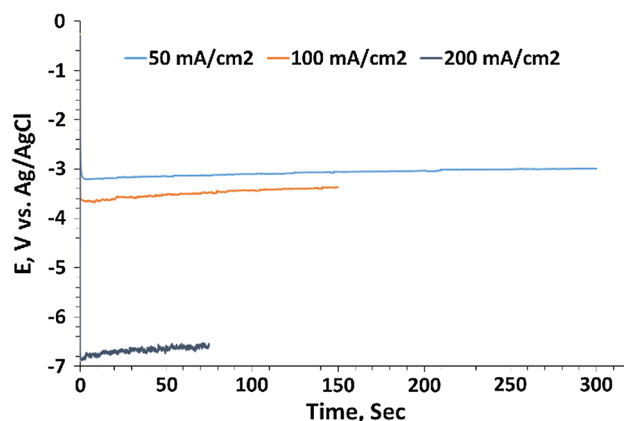

Figure 6 Potential versus time curves of Sn electrodeposition at few current densities (18 mM SnCl$_2$/50 mM SC solution, 15 C).

(Fig. 6). The morphology of the corresponding electrodes is depicted in the SEM images in Fig. 7. At a cathodic current density of 50 mA/cm^2, the deposition process starts at −3.2 V and gradually (after 200 s) the potential stabilizes at around −3 V, along with the increase of the surface area. Morphological comparison of the two electrodes electrodeposited under potentiostatic and galvanostatic regimes (Figs. 5d, 7a, respectively) reveals vertically oriented nanotrees with an incomplete coverage of gaps
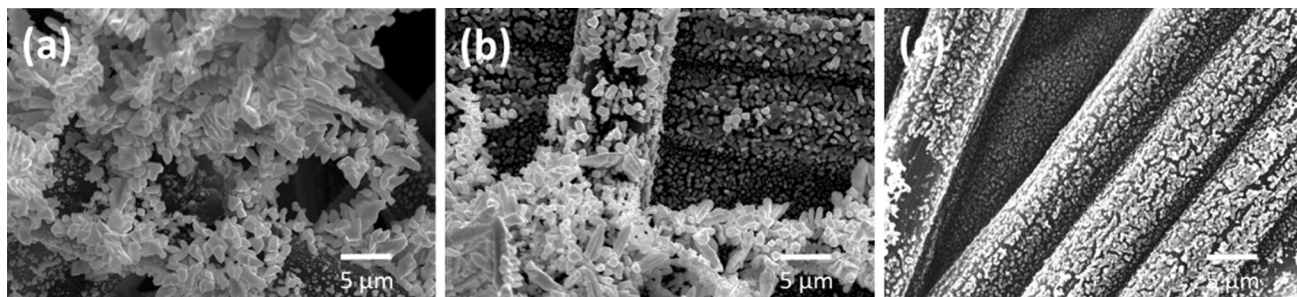
Figure 7 SEM micrographs of electrodeposited Sn at the current densities of **a** 50 mA/cm², **b** 100 mA/cm², and **c** 200 mA/cm², corresponding with the data presented in Fig. 6.

between clusters. However, the dendrites formed under galvanostatically controlled experiments are less developed. This is due to the gradual increase of the potential (lower overpotentials) during the galvanostatic electrodeposition process, as can be seen in Fig. 6. Similar differences were shown for Cu electrodeposition by Popov et al. [37]. When a higher current density of 100 mA is applied, the reduction occurs at more negative potentials in the vicinity of −3.5 V and fewer dendrites are seen. Moreover, applying 200 mA/cm² (Fig. 7c) results in electro-reduction under the potential of nearly −7 V. This shows the formation of a larger number of nucleation sites and growth occurring laterally and without the formation of TBS. It should be remembered that at such a low potential of nearly −7 V, most of the charge is consumed by the hydrogen evolution process, which gives rise to small nuclei formation processes over particle growth. Hydrogen gas covering the surface reduces the effective electrode area and increases significantly the cathodic potential to −7 V.

Influence of additives

Ionic surfactants are widely used as templating agents for the fabrication of controlled shaped nanostructure materials [38, 39]. We have examined this approach as a means of further controlling the morphology of the deposited TBS. Two commonly used surfactants were selected: cationic HDTAB (hexadecyltrimethylammonium bromide) and anionic SDS (sodium dodecyl sulfate).

Prior to these experiments, the diffusion coefficients of Sn^{2+} ions in HDTAB, SDS, and sodium citrate (SC) solutions were calculated from chronoamperometric measurements, at −0.9 V

versus Ag/AgCl to avoid hydrogen evolution, using the Cottrell equation:

$$i(t) = \frac{nFAD_R^{1/2}C_R^*}{\pi^{1/2}t^{1/2}}, \tag{1}$$

where n is the number of electrons, F is the Faraday constant, A is the electrode surface area, D_R is the diffusion coefficient, and C_R^* is the reductant (Sn^{2+}) bulk concentration. The calculated diffusion coefficient values of Sn^{2+} in solution containing SC, SDS, and HDTAB were 1.50×10^{-5}, 4.70×10^{-6} and 2.55×10^{-5} cm²/s, respectively. These results suggest that bulky SDS anion solvates the Sn^{2+} and significantly reduces the diffusion coefficient compared to SC and HDTAB under the same conditions.

As described above, at high overpotentials, the Sn morphology is entirely controlled by diffusion due to depletion of Sn–citrate complex from the electrode surface. Added anionic surfactant, such as SDS, solvates the Sn^{2+} ions as indicated by the significantly smaller diffusion coefficient compared to SC. However, when HDTAB is added, an increase in the diffusion coefficient can be observed, which is in line with minimal interaction with the positively charged Sn^{2+} ions.

The influence of these surfactants on the morphology of electrodeposited Sn was studied under potentiostatic polarization to −3 V (vs. Ag/AgCl), limited by a predefined charge condition of 2 C (Fig. 8a–c). By means of comparison, we show that at early stages of the cathodic process, the nucleation seeds growing in the absence of surfactants (Fig. 8a) or with HDTAB (Fig. 8c) almost fully cover the surface, in line with their higher diffusion coefficient. Conversely, in the presence of SDS, a bulky negatively charged surfactant which interacts with the positively charged Sn^{2+} ions, the surface density of
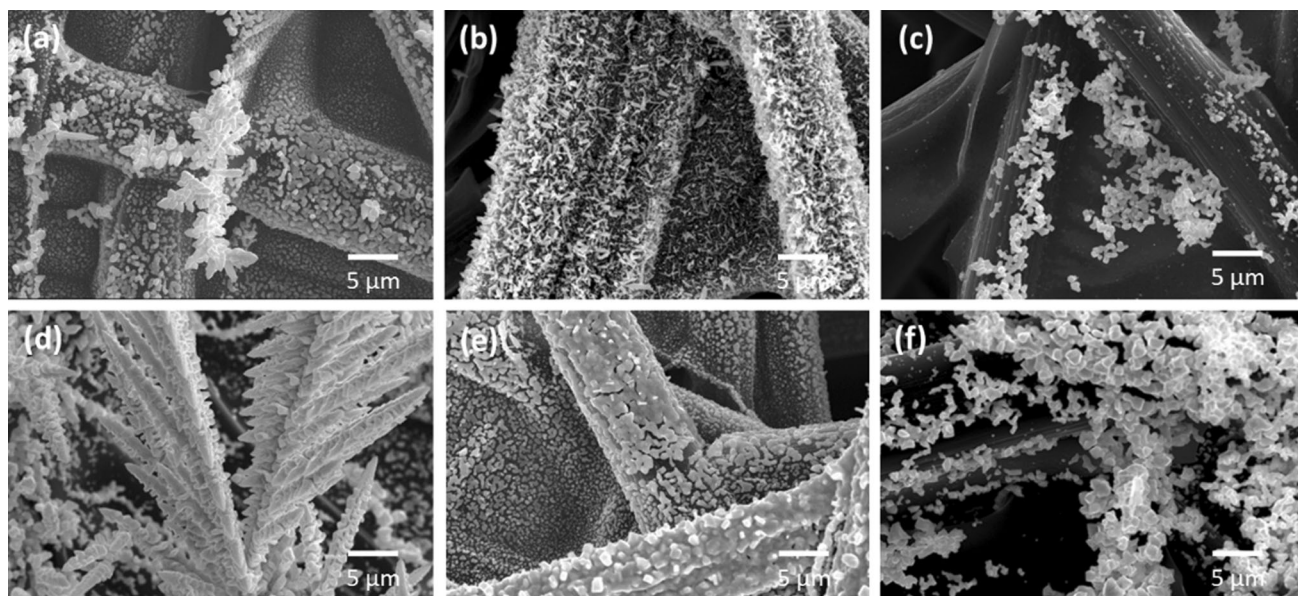
Figure 8 Sn continues electrodeposition in the presence of **a** 50 mM SC, **b** 1 mM HDTAB, and **c** 1 mM SDS and pulse electrodeposition of 2 s at −3 V followed by 5-s rest in the same solutions (**d–f**, respectively) (18 mM SnCl$_2$, −3 V, 2 C).
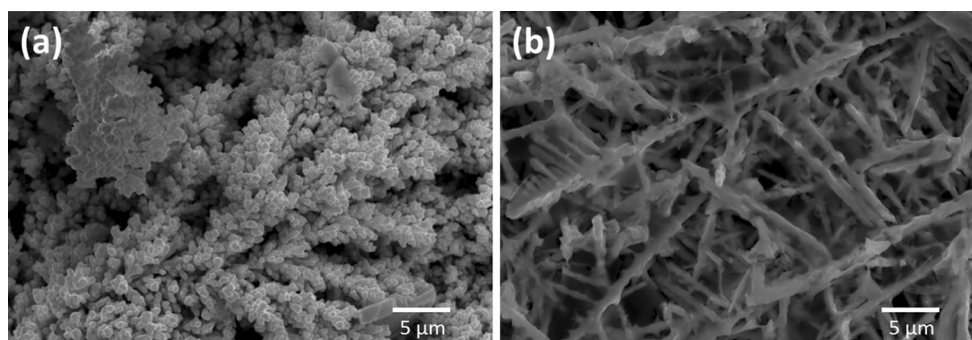

Figure 9 SEM micrographs of Sn electrodeposition in **a** 0.1 M and **b** 0.5 M HCl solutions at −0.9 V (15 C).

the nuclei is smaller and most of the carbon fiber surface remains free from aggregates (Fig. 8b). Further growth of these seeds clearly shows an increase in the size of the original seeds. Interestingly, in the case of HDTAB relatively uniform coverage of needle-like metallic Sn is seen, resulting from lateral growth (Fig. 8c). This behavior is ascribed to the interaction of the HDTA$^+$ ions with the negatively charged electrode, thereby reducing the process kinetics and improving the coverage [40].

In light of the slow diffusion of tin reactants in the presence of SDS and the low surface coverage, we have applied a pulse current method that consisted of

a 2-s pulse at 50 mA/cm^2 followed by a 5-s rest ($i = 0$). The accumulated charge was limited to 2 coulombs. Using pulse deposition, higher surface nucleation density, higher surface coverage, and lower porosity can be attained [41]. Careful control of the pulse frequency and duty cycle was reported as a means of forming smaller nanometric crystallites [42]. Figure 8d–f shows the morphology of the Sn electrode obtained in similar solutions containing SC, HDTAB, and SDS using a current pulse method. An obvious increase of the particle size and surface coverage is seen in comparison to the equivalent electrodes formed by a continuous deposition

method (Fig. 8a–c). A pulsing effect in the presence of HDTAB further smoothened the deposited tin to a nearly full coverage.

By applying potential pulses of only 2 s followed by a long enough rest time of 5 s, the Sn^{2+} concentration in the vicinity of the electrode replenishes itself. During this rest period, the positively charged HDTAB molecules adsorbed on the freshly deposited Sn, which further grows laterally until the particles merge to form a uniform coating. Despite their slower diffusion, SDS-solvated Sn^{2+} ions, similar to citrate coordinated ions, have sufficient time to reach the electrode during the 5 s rest time. Hence, the surface coverage is more uniform in the pulse deposition (Fig. 8f) compared to continuous deposition (Fig. 8c).

Acid effect on Sn morphology

The pH effect on the Sn electroplating was studied by Han et al., using low overpotentials and selected pH of relevance to this study (pH 0–4) [26]. At pH lower than 1.2, the deposition proceeded in a faster kinetics than at high pH, producing non-uniform coating. In this study, the standard solution bath comprised 18 mM $SnCl_2$ and 50 mM SC at pH 6. Our approach was to control the dimensions of the nanotrees and increase their roughness at low pH by adding HCl.

Standard plating baths containing 0.1 M and 1 M HCl as additives were used for Sn reduction at −0.9 V. This potential was chosen to minimize the hydrogen evolution process. Figure 9 shows SEM micrographs of the Sn structures attained under these strong acidic conditions (pH = 0 to 1). Sn nanotrees formed at pH 1 have highly roughened surfaces (Fig. 9a), which is completely different than the one presented above (Fig. 5a), consisting of only large relatively smooth particles. Further change of the morphology is seen in the plating from the solution with 1 M HCl, depicting highly branched dendrites seemingly interconnected in a grid-like form. In addition, the dendrites retain tree-like shapes, with a steam length of 5–40 μm and a diameter of 1.5 μm or less.

The influence of an acid additive on Sn morphology is explained as a combination of two processes. The first is caused by the shift in Sn^{2+}/Sn redox potential to a more positive value. This is based on *Han* and *Ivey*, who reported a positive shift of about 135 mV in Sn plating potential, when the solution pH

was changed from 4.1 to 1.1 [26]. In our measurements, where the pH was changed from 6 in the standard 18 mM $SnCl_2$/50 mM SC solution to 0 in the 1 M HCl solution, a matching positive shift of 200 mV was observed. At pH < 1 and an applied potential of −0.9 V, the practical overpotential is 750 mV, thereby driving the reaction towards mass transport control rather than kinetic control seen at pH 6 (Fig. 5), thus facilitating the formation of dendritic deposition.

The second process promoted by HCl etching of metallic structures at pH below 1 is occurring during the reduction [24]. This behavior leads to roughening of the sharp TBS edges in 0.1 M HCl (Fig. 9a), or nearly complete removal of their branches and other small features on the remaining branches, seen in Fig. 9b in the case of 1 M HCl. It should be emphasized that the dissolution occurs on the stem as well, resulting in thinning of the stem to an average width of less than 1 μm. The dissolved Sn^{2+} ions enrich the electrode vicinity and are reduced back to their metallic form, seen as a fine skin connecting the nanotrees and their branches (Fig. 9b). The mechanism describing these processes is illustrated schematically in Fig. 10. To the best of our knowledge, this type of two-dimensional Sn nanostructure has not been reported before and will be further explored in our future work.

The strong impact of the acids on the TBS morphology was further studied using QCM and EQCM measurements. In these experiments, a fixed amount of Sn (estimated as 7000 ng) was reduced on a gold-coated quartz crystal electrode using a procedure described in Fig. 11a. A typical plot describing the current and QCM frequency (Δf) change during the Sn film formation is shown in Fig. 11a. A gradual decrease of crystal frequency is observed corresponding to the accumulation of metallic Sn on the electrode. The calculated equivalent mass per electron (M.P.E) is 110 gr eq^{-1} compared with 59.3 gr eq^{-1} of bulk Sn reduction by 2e$^-$. This large difference is attributed to a well-documented effect of the roughness of QCM, which is reflected in deviation from Sauerbrey's equation [43]:

$$\Delta f = -\frac{2f_0}{A\sqrt{\rho_q \mu_q}}\Delta m, \qquad (2)$$

where f_0 is the resonant frequency (Hz), Δf is the frequency change (Hz), Δm is the mass change (g), A is the piezoelectrically active crystal area (area
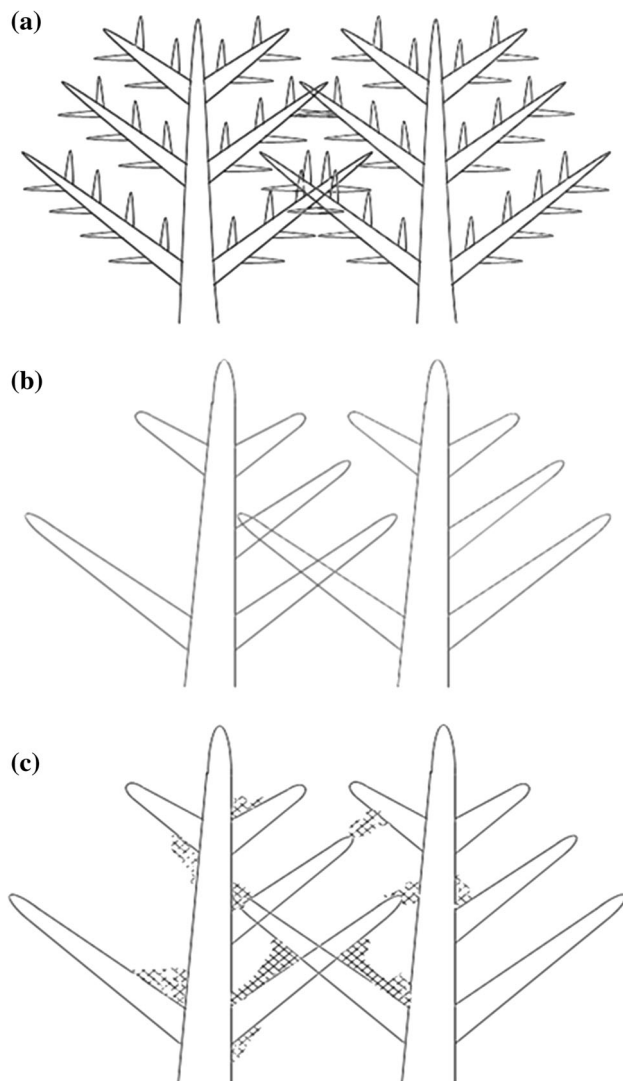
(a)

(b)

(c)

Figure 10 Schematic presentation of Sn electrodeposition process under strong acidic conditions (pH 0). **a** Sn deposition forms dendritic tree-like nanostructures; **b** Sn etching due to the high acid concentration; and **c** reduction of the dissolved Sn^{2+} ions as a fine skin connecting the nanotrees and their branches.
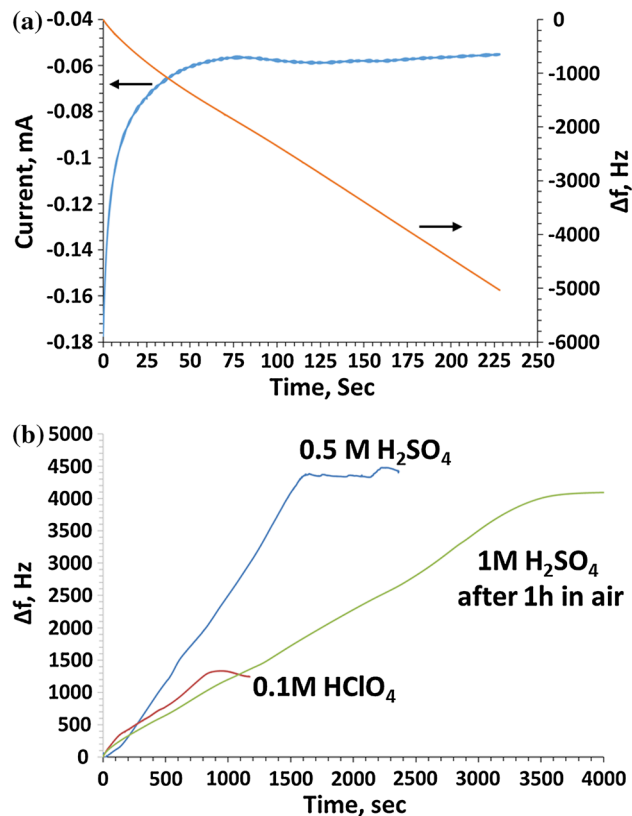
(a)

(b)

Figure 11 **a** Typical EQCM measurement of Sn electrodeposition on gold-coated quartz crystal electrode and **b** QCM measurements of the Sn electrodeposited electrodes after immersion in various acidic solutions.

between the electrodes, cm^2), ρ_q is the density of quartz ($\rho_q = 2.648$ g/cm^3), and μ_q is the shear modulus of quartz for AT-cut crystal ($\mu_q = 2.947 \times 10^{11}$ g cm^{-1} s^{-2}). Sauerbrey's equation only applies to systems where the deposited mass is distributed evenly and has low roughness. Therefore, the large deviation in equivalent mass of Sn in TBS is expected.

The reactivity of TBS deposited on QCM gold surface towards acids was explored under three conditions: (1) immersion of a freshly prepared electrode in 0.5 M H_2SO_4 solution, (2) immersion in the same solution after exposure for one hour to air, and (3) immersion in 0.1 M $HClO_4$. The QCM results are depicted in Fig. 11b. Upon immersion of the coated electrodes in acid solutions, Δf increases rapidly due to extensive dissolution of the Sn layer. After exposure of the freshly prepared metallic surface to the air, the corrosion process slows down significantly. However, after 3000 s the dissolution process ends with a complete removal of Sn. Interestingly, when the electrode was immersed in 0.1 M $HClO_4$, the increase of the frequency change stops after 800 s with only 25 % change of the total frequency acquired during the deposition ($\Delta f = 7000$ Hz). We attribute this behavior to the formation of a stable passivation layer on the electrodeposited surface, which could not be detected by SR-FTIR analysis. Even more importantly, subsequent immersion of this pretreated electrode in 0.5 M H_2SO_4 solution failed to show any substantial frequency change.

Conclusions

Tin branched structures (TBSs) were prepared by a controlled template-free electrodeposition process. Hierarchical shapes of metallic Sn particles formed directly on Sn, a porous carbon substrate. In this study, we have shown that a proper selection of potentiostatic and galvanostatic conditions, as well as the choice of additives, can enable good control over the morphology and the efficiency of the deposition process. Variation of the electrodeposition from −0.9 V to 1.5 V and above shifts the morphology from lateral growth of smooth facet particles that occurs under kinetic control and low overpotentials to hierarchical branched Sn dendrites under high overpotentials, known to be ascribed to mass transfer limiting currents. The corresponding decrease of the columbic efficiency is attributed to the increasing hydrogen evolution rates at high overpotentials, which also interfere with the initial nucleation process and therefore assist in directing the growth on these nuclei.

Surfactants are evaluated in this work as additives that can regulate the reduction rate and mitigate the effect of mass transport limits. This approach was considered as a means of increasing the diffusion coefficient of solvated Sn^{+2} or as a way to slow down the reaction kinetics. Using positively charged surfactants affects mostly the metallic surfaces, while negatively charged surfactants interfere with the diffusion of Sn^{2+} ions and lead to the formation of larger branched Sn particles. Further control of these particles' morphology is attained by using HCl as an additive at selected concentrations. A strong impact of acid addition on electrodeposition morphology is identified. TBS forms under HCl solutions at relatively low overpotentials due to the positive shift of the electrodeposition potential as well as vast hydrogen evolution. The reduction of Sn^{2+} ions from 1 M HCl electroplating solution induces two distinct morphological changes: (1) etching of the freshly deposited TBS and (2) formation of thin metallic skin between the remaining networks of Sn. Supporting EQCM study of the influence of H_2SO_4 and $HClO_4$ additives on the electrodeposited Sn shows that immersion in 0.1 M $HClO_4$ solution stabilizes the Sn surface and stops the dissolution process. Hence, it can be used in more gentle etching procedures of high-surface area deposited metallic tin.

References

[1] Sun Z, Cao C, Han W-Q (2015) A scalable formation of nano-SnO_2 anode derived from tin metal-organic frameworks for lithium-ion battery. RSC Adv 5:72825–72829. doi:10.1039/C5RA12295C

[2] Meyyappan M (2013) Nanostructured materials for supercapacitors. J Vac Sci Technol Vac Surf Film 31:050803. doi:10.1116/1.4802772

[3] Candelaria SL, Shao Y, Zhou W et al (2012) Nanostructured carbon for energy storage and conversion. Nano Energy 1:195–220. doi:10.1016/j.nanoen.2011.11.006

[4] Novikov A, Nowottnick M (2012) Characterization of nanoscaled solder material. Phys status solidi 209:819–824. doi:10.1002/pssa.201100541

[5] Wang Y, Zhao X, Xie X et al (2015) Effects of nano-SiO2 particles addition on the microstructure, wettability, joint shear force and the interfacial IMC growth of Sn3.0Ag0.5Cu solder. J Mater Sci Mater Electron. doi:10.1007/s10854-015-3151-8

[6] Ma H, Teng K, Fu Y et al (2011) Synthesis of visible-light responsive Sn–SnO_2/C photocatalyst by simple carbothermal reduction. Energy Environ Sci 4:3067–3074. doi:10.1039/C1EE01095F

[7] Agashe C, Takwale MG, Marathe BR, Bhide VG (1988) Structural properties of SnO_2: F films deposited by spray pyrolysis. Sol Energy Mater 17:99–117. doi:10.1016/0165-1633(88)90010-X

[8] Zhang W, Zeng W, Miao B (2015) Preparation of SnO_2 nanoflower with porous nanosheet via a one-step hydrothermal method. Mater Lett 158:377–379. doi:10.1016/j.matlet.2015.06.056

[9] Das S, Jayaraman V (2014) SnO_2: a comprehensive review on structures and gas sensors. Prog Mater Sci 66:112–255. doi:10.1016/j.pmatsci.2014.06.003

[10] Dattoli EN, Wan Q, Guo W et al (2007) Fully transparent thin-film transistor devices based on SnO_2 nanowires. Nano Lett 7:2463–2469. doi:10.1021/nl0712217

[11] Kaushik V, Sharma H, Vankar VD (2012) Recent developments in the growth and properties of carbon nanotubes and carbon nanostructures: a review. Int J Green Nanotechnol 4:534–540. doi:10.1080/19430892.2012.738508

[12] Villain S, Knauth P, Schwitzgebel G (1997) Electrodeposition of nanocrystalline silver: study of grain growth by

measurement of reversible electromotive force. J Phys Chem B 101:7452–7454. doi:10.1021/jp970330e

[13] Wirtz M, Parker M, Kobayashi Y, Martin CR (2002) Template-synthesized nanotubes for chemical separations and analysis. Chem Eur J 8:3572–3578. doi:10.1002/1521-3765(20020816)8:16<3572:AID-CHEM3572>3.0.CO;2-9

[14] Sloan J, Wright DM, Bailey S et al (1999) Capillarity and silver nanowire formation observed in single walled carbon nanotubes. Chem Commun. doi:10.1039/A901572H

[15] Prieto AL, Martín-González M, Keyani J et al (2003) The electrodeposition of high-density, ordered arrays of Bi1-xSbx nanowires. J Am Chem Soc 125:2388–2389. doi:10.1021/ja029394f

[16] Saejeng Y, Tantavichet N (2009) Preparation of Pt–Co alloy catalysts by electrodeposition for oxygen reduction in PEMFC. J Appl Electrochem 39:123–134. doi:10.1007/s10800-008-9644-x

[17] Shin H-C, Dong J, Liu M (2003) Nanoporous structures prepared by an electrochemical deposition process. Adv Mater 15:1610–1614. doi:10.1002/adma.200305160

[18] Xiang J, Liu B, Wu S-T et al (2005) A controllable electrochemical fabrication of metallic electrodes with a nanometer/angstrom-sized gap using an electric double layer as feedback. Angew Chem Int Ed 44:1265–1268. doi:10.1002/anie.200461797

[19] Ye W, Yan J, Ye Q, Zhou F (2010) Template-free and direct electrochemical deposition of hierarchical dendritic gold microstructures: growth and their multiple applications. J Phys Chem C 114:15617–15624. doi:10.1021/jp105929b

[20] Wang J, Wei L, Zhang L et al (2012) Zinc-doped nickel oxide dendritic crystals with fast response and self-recovery for ammonia detection at room temperature. J Mater Chem 22:20038–20047. doi:10.1039/C2JM34192A

[21] Li G-R, Xu H, Lu X-F et al (2013) Electrochemical synthesis of nanostructured materials for electrochemical energy conversion and storage. Nanoscale 5:4056–4069. doi:10.1039/C3NR00607G

[22] Despić AR, Popov KI (1972) Transport-controlled deposition and dissolution of metals. In: Conway BE, Bockris JO (eds) Modern aspects of electrochemistry No. 7 SE-4. Plenum Press, New York, pp 199–313

[23] Diggle JW, Despić ARBJ (1969) The mechanism of the dendritic electrocrystallization of zinc. J Electrochem Soc 116:1503–1514

[24] Nikolić ND, Popov KI (2010) Hydrogen Co-deposition effects on the structure of electrodeposited copper In: Djokic SS (ed) Modern aspects of electrochemistry No. 48. Springer, Berlin, pp 1–70. doi:10.1007/978-1-4419-5589-0

[25] Bicelli LP, Bozzini B, Mele C, D'Urzo L (2008) A review of nanostructural aspects of metal electrodeposition. Int J Electrochem Sci 3:356–408

[26] Han C, Liu Q, Ivey DG (2008) Kinetics of Sn electrodeposition from Sn(II)–citrate solutions. Electrochim Acta 53:8332–8340. doi:10.1016/j.electacta.2008.06.037

[27] Jeun J-H, Kim W-S, Hong S-H (2013) Electrophoretic deposition of carbon nanoparticles on dendritic Sn foams fabricated by electrodeposition. Mater Lett 112:109–112. doi:10.1016/j.matlet.2013.09.002

[28] Krichevski O, Teller H, Subramanian P, Schechter A (2015) The synthesis of metallic β-Sn nanostructures for use as a novel Pt catalyst support and evaluation of their activity toward methanol electrooxidation. Electrocatalysis. doi:10.1007/s12678-015-0273-y

[29] Elbasiony AMR, El Abedin SZ, Endres F (2014) Electrochemical synthesis of freestanding tin nanowires from ionic liquids. J Solid State Electrochem 18:951–957. doi:10.1007/s10008-013-2340-8

[30] Mackay D, Janish M, Sahaym U et al (2014) Template-free electrochemical synthesis of tin nanostructures. J Mater Sci 49:1476–1483. doi:10.1007/s10853-013-7917-1

[31] Owen CD, Norton MG (2016) Growth mechanism of one dimensional tin nanostructures by electrodeposition. J Mater Sci 51:577–588. doi:10.1007/s10853-015-9323-3

[32] Bearfield DW, Greenwood EA, Warwick ME (1983) Laboratory studies of the corrosion of side-seams in soldered tinplate containers: part II. The role of the solder and the electrolyte. Br Corros J 18:51–54. doi:10.1179/000705983798274092

[33] Witten TA, Sander LM (1981) Diffusion-limited aggregation, a kinetic critical phenomenon. Phys Rev Lett 47:1400–1403

[34] Lee B-Z, Lee DN (1998) Spontaneous growth mechanism of tin whiskers. Acta Mater 46:3701–3714. doi:10.1016/S1359-6454(98)00045-7

[35] Nikolić N, Branković G, Lačnjevac U (2012) Formation of two-dimensional (2D) lead dendrites by application of different regimes of electrolysis. J Solid State Electrochem 16:2121–2126. doi:10.1007/s10008-011-1626-y

[36] Gileadi E (2011) Physical Electrochemistry. WILEY-VCH Verlag GmbH & Co. KGaA, Weinheim, pp 98–99

[37] Popov KI, Pavlović MG, Maksimović MD, Krstajić SS (1978) The comparison of galvanostatic and potentiostatic copper powder deposition on platinum and aluminium electrodes. J Appl Electrochem 8:503–514. doi:10.1007/BF00610795

[38] Murphy CJ, Sau TK, Gole AM et al (2005) Anisotropic metal nanoparticles: synthesis, assembly, and optical

applications. J Phys Chem B 109:13857–13870. doi:10.1021/jp0516846

[39] Xiao J, Qi L (2011) Surfactant-assisted, shape-controlled synthesis of gold nanocrystals. Nanoscale 3:1383–1396. doi:10.1039/C0NR00814A

[40] Gileadi E (2011) Physical Electrochemistry. WILEY-VCH Verlag GmbH & Co. KGaA, Weinheim, pp 297–302

[41] Popov KI, Maksimovic MD (1989) Theory of the effect ofelectrodeposition at a periodically changing rate on the morphology of metal deposits. In: Conway BE, Bockris JO'M, White RE (eds) Modern aspects of electrochemistry, vol 19. Plenum, New York and London, pp 193–251

[42] Popov KI, Maksimović MD, Totovski DĆ (1982) Fundamental aspects of pulsating current metal electrodeposition VI: the comparison of electrode surface roughening in pulsating current and periodic reverse current electrodeposition of metals. Surf Technol 17:125–129. doi:10.1016/0376-4583(82)90014-0

[43] Gileadi E (2011) Physical Electrochemistry. WILEY-VCH Verlag GmbH & Co. KGaA, Weinheim, pp 253–264